Effects of entrance channels on breakup fusion induced by ¹⁹F projectiles

Amritraj Mahato ⬤, Dharmendra Singh ⬤,[*] Nitin Sharma ⬤, Pankaj K. Giri, and Sneha B. Linda
Department of Physics, Central University of Jharkhand, Ranchi 835222, India

Harish Kumar, Suhail A. Tali ⬤, M. Afzal Ansari ⬤, and Asif Ali
Department of Physics, Aligarh Muslim University, Aligarh 202002, India

Nabendu Kumar Deb ⬤
Department of Physics, Gauhati University, Guwahati, Assam 781014, India

N. P. M. Sathik
Department of Physics, Jamal Mohamed College, Tiruchirappalli 620020, India

S. Kumar, R. Kumar, S. Muralithar, and R. P. Singh ⬤
Inter University Accelerator Centre, Aruna Asaf Ali Marg, New Delhi 110067, India

The study of breakup fusion of ¹⁹F with ¹⁵⁴Sm target was studied through offline γ ray spectrometry. Partial cross sections of evaporation residues produced in this reaction were measured in center-of-mass energies ranging $\approx$3–30 MeV above the fusion barrier. The excitation functions of the evaporation residues populated through xn/pxn channels were found to be satisfactorily reproduced by statistical model calculations, whereas for the α emitting channels the cross sections show an enhancement over the theoretical predictions. The critical angular momentum deduced from the measured cross sections was found to be in good agreement with statistical model calculations. The degree of fusion incompleteness in the ¹⁹F + ¹⁵⁴Sm reaction is estimated by comparing the fusion excitation functions with coupled channels calculations and the extracted fusion function with the universal fusion function. The large cross sections observed for incomplete fusion products support the interpretation that this suppression of fusion is caused by ¹⁹F breaking up into charged fragments before reaching the fusion barrier. The incomplete fusion probability was also found to increase with the reduced mass and charge of the entrance channel, indicating the influence of entrance channel mass asymmetry and Coulomb repulsion on incomplete fusion. The present analysis shows the presence of strong clustering in the ¹⁹F projectile as α and ¹⁵N.

I. INTRODUCTION

The characteristics of α cluster states in heavy ions (HIs) are very important for understanding nuclear processes in stars. For energies far below the Coulomb barrier (of astrophysical interest), very small cross sections cannot be measured in laboratories. The details of the interaction between the cluster and regular states must be known for the deduction of such cross sections, since strong α cluster states can increase the α width to states that are closer to the region of astrophysical interest through configuration mixing [1]. In general, the $N = Z$, even-even nuclei such as ⁸Be, ¹²C, ¹⁶O, and ²⁰Ne are associated with strong clustering. It has proved to be far more difficult to study clustering phenomena in $N \neq Z$ nuclei because the "extra" nucleons introduce additional degrees of freedom [2,3]. The α decay threshold is usually lower in energy than the nucleon decay threshold in even-even

$N = Z$ nuclei. However, for $N \neq Z$ nuclei the energy thresholds for neutron and α decay are close. The closeness of the decay thresholds for $N \neq Z$ nuclei may provide new insight to understand the interplay between the single-particle and cluster degrees of freedom. At present, data on the α cluster states in $N \neq Z$ nuclei (like ¹⁹F, ²¹Ne, etc.) are scarce due to complications in experiments and data analysis [4]. As such, the spectroscopy of ¹⁹F is of interest for nuclear astrophysics and nuclear structure [5]. In astrophysics, fluorine and the reactions producing and destroying it play a key role in constraining models of stars in different evolutionary stages, such as the asymptotic giant branch (AGB) stars, responsible of the production of about half of the elements heavier than Fe [6]. In nuclear structure, ¹⁹F has been subject to investigations [7] aiming at the identification of α and more exotic cluster structures. Also, its spectroscopy is very useful to constrain the nuclear properties of the ¹⁹Ne mirror nucleus.

Several studies existing in the literature [8–11] show that there is a significant contribution of incomplete fusion (ICF)

*dsinghcuj@gmail.com

of $N = Z$ projectiles (like ^{12}C, ^{16}O, and ^{20}Ne etc.) at energies above the Coulomb barrier. The study of ICF of such projectiles has been done through different types of measurements; such as excitation functions (EFs) [9–11], forward recoil range distributions (FRRDs) [12,13], angular distributions [13], and spin distributions [14–16]. However, the studies of ICF on $N \neq Z$ projectiles (like ^{19}F) are limited to few systems [17–19]. The study of ICF reaction dynamics has taken a central place in the field of nuclear physics research in the past few years, since the mechanism involved in these reactions is still only partially understood, especially in terms of the angular momentum involved in the population of evaporation residues (ERs) [14–16]. Recently, the study of ICF in the ^{14}N + ^{181}Ta system was reported [20]. A significant amount of breakup is found in the ^{14}N projectile, which is an $N = Z$ odd-odd nucleus. The ICF contribution was found to depend strongly on projectile energies, the product of projectile and target charges, and α Q value of the projectile.

In this work, the measured data on the excitation functions (EFs) for ^{19}F + ^{154}Sm system at above barrier energies through offline stacked foil activation technique followed by offline γ ray spectrometry are presented. The measured EFs were then analyzed within the framework of the standard statistical model code PACE-4 [21,22]. The analysis of EF data suggests the presence of α cluster states in ^{19}F nuclei. It was also found that there is a significant contribution of incomplete fusion (ICF) of ^{19}F projectile with ^{154}Sm target along with its complete fusion (CF) at above-barrier energies. In case of ICF, the ^{19}F projectile breaks up into ^{15}N + α or ^{11}B + 2α, before fusing with the target ^{154}Sm. The fragments ^{15}N or ^{11}B then fuse with the target ^{154}Sm, while the α particle(s) moves as spectator. The influence of entrance channel mass asymmetry and Coulomb repulsion on ICF was investigated through reduced mass and reduced charge of the dinuclear system. Further, an effort was also made to study the effect of breakup on the fusion cross sections through the standard formulation of the universal fusion function (UFF) [23]. The present paper is organized as follows: A brief description of the experimental techniques is given in Sec. II, the details of the analysis of data and its interpretation are given in Sec. III, and a summary of the present work is presented in Sec. IV.

II. EXPERIMENTAL TECHNIQUES

Measurements were carried out at Inter University Accelerator Centre (IUAC), New Delhi, India [24,25] using the 15 UD Pelletron accelerator facility. An energetic beam of ^{19}F was used to bombard on the stack of ^{154}Sm targets of thickness $\approx$200–500 μg/cm^2 with aluminum (Al) backings [26] of thickness $\approx$1.0–1.5 mg/cm^2. The Al backings (catcher foils) were used to trap the recoiling evaporation residues (ERs). The thickness of each Al catcher and target foil was determined prior to use by weighing as well as by the α transmission method. The ^{19}F^{8+} beam of diameter $\approx$4 mm was collimated on a stack of ^{154}Sm. This stack was irradiated for about 9 hours with varying beam current $\approx$10–15 nA, keeping in view the lifetimes of the populated ERs. The beam current was monitored behind the target-catcher assembly with an electron suppressed Faraday cup, using a current

TABLE I. Measured ERs produced via different reaction channels in the ^{19}F + ^{154}Sm system at $E_{lab} \approx 78$–110 MeV along with their spectroscopic data [27,28].

Serial No.	Reaction channel	Half-life	$E\gamma$ (keV)	B_R (%)
1.	^{154}Sm$(F, 4n)$ ^{169}Lu	34.06 h	191	20.60
			379	2.11
			165	1.97
2.	^{154}Sm$(F, 5n)$ ^{168}Lu	6.70 min (m)	111	49.00[a]
			228	7.00[a]
			348	6.70[a]
		5.50 min (g)	199	76.00[a]
			979	15.70[a]
			896	9.00[a]
			885	7.70[a]
3.	^{154}Sm$(F, 6n)$ ^{167}Lu	51.50 min	239	8.60
			214	3.60
			179	2.80
4.	^{154}Sm$(F, p5n)$ ^{167}Yb	17.50 min (m)	115	55.40
			176	21.00
5.	^{154}Sm$(F, \alpha3n)$ ^{166}Tm	7.70 h (m)	779	18.90
			183	16.10
			705	10.96
6.	^{154}Sm$(F, \alpha4n)$ ^{165}Tm	30.06 h	243	35.50
			297	12.71
7.	^{154}Sm$(F, \alpha5n)$ ^{164}Tm	5.10 min	208	14.60
			317	10.00
8.	^{154}Sm$(F, 2\alpha3n)$ ^{162}Ho	1.13 h	187	28.60
			283	11.30
9.	^{154}Sm$(F, 2\alpha4n)$ ^{161}Ho	2.48 h	211	46.00

[a]Relative intensity.

integrator device. The irradiation of the ^{154}Sm target stack was carried out in the General Purpose Scattering Chamber (GPSC), which has an in-vacuum transfer facility to minimize the lapse time between the stop of the irradiation and beginning of the counting of samples. The γ activity induced in each sample was recorded after the irradiation of the target foils using a high purity germanium (HPGe) detector coupled to a CAMAC based data acquisition system developed by IUAC, New Delhi. The HPGe detector was precalibrated using standard γ ray sources (^{152}Eu and ^{133}Ba). The γ ray activity built up in each irradiated sample was recorded for multiple time intervals ranging from 5 min to several hours to trap the maximum residues as possible. The resolution of the HPGe detector was found to be 2.5 keV for a 1408 keV γ ray from the ^{152}Eu source. Table I shows a list of identified ERs in the ^{19}F + ^{154}Sm reaction at projectile energies $E_{lab} \approx 78$–110 MeV. The activity of the measured ERs populated was extracted from the recorded γ ray spectra. Figure 1 shows a typical recorded γ ray energy spectrum for the present system at $E_{lab} \approx 109.4$ MeV, recorded for 300 s and 20 min after the ending of the beam irradiation. In this spectrum, the peaks were assigned to the respective identified ERs, on the basis of their characteristic γ rays as well as from their decay curve analysis. The background spectrum of Al backing only was also recorded in the experiment. The γ ray peaks of observed
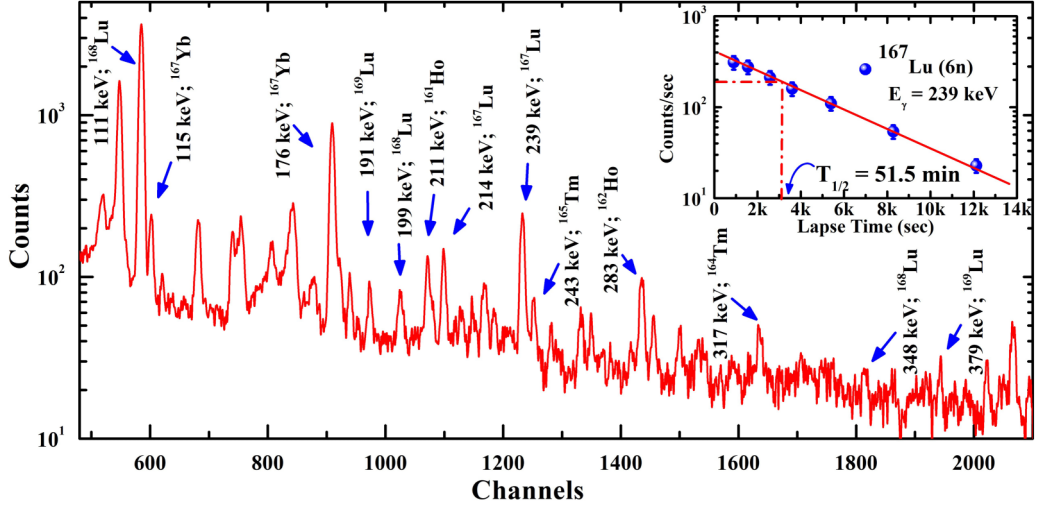
FIG. 1. Typical γ ray spectrum of the residues populated in the ^{19}F + ^{154}Sm system at $E_{lab} \approx 109.4$ MeV, recorded for about 300 s and 20 min after the ending of irradiation of stack.

ERs were found to be absent in the background spectrum obtained. The half-lives of residues extracted from the measured data were found to be in good agreement with the standard database [27,28]. As a representative case, the decay curve of the residue ^{167}Lu having half-life of 51.50 min is displayed in the inset of Fig. 1. The production cross sections σ_{ER} of the measured ERs were calculated using the standard formulation [29], given as

$$\sigma_{ER} = -\frac{A\lambda \exp(\lambda t_{lps})}{N_0 \phi B_R k_{sac} \epsilon [1 - \exp(-\lambda t_{ird})][1 - \exp(-\lambda t_{cnt})]},$$

(1)

where A is the total number of counts in the photo-peak recorded in irradiation time t_{ird}, λ is the decay constant of the residue, N_0 is the total number of target nuclei, B_R is the branching ratio of the identified γ ray, ϕ is the flux of the incident beam, ϵ is the geometry dependent efficiency of the HPGe detector, t_{lps} is the time elapsed between the stop of irradiation and start of the counting, t_{cnt} is the counting time, and $k_{sac} = [1 - e^{-\mu_c d}]/\mu_c d$ is the self-absorption correction factor for the target of thickness d with absorption coefficient μ_c. Further details regarding the experimental setup and cross section measurement can be found in Ref. [9].

Several factors are responsible for the uncertainties in the measured cross sections. The main factors are the following: (i) the error arising from the fluctuations in beam current was estimated to be less than 6%, (ii) the uncertainty in the efficiency calibration of the HPGe detector was estimated to be less than 5%, (iii) the uncertainty due to the nonuniformity of the target and thickness measurement was estimated to be less than 3%, (iv) to minimize the error, the counting was done for dead time below 10%, and (v) uncertainty due to the straggling effect of the projectile passing through the stack was estimated to be less than 2%. The overall uncertainties from various factors including statistical errors in the photopeak area are estimated to be less than 15%.

III. RESULTS AND ANALYSIS

In the present measurements, a total of nine ERs, namely, ^{169}Lu (4n), ^{168}Lu (5n), ^{167}Lu (6n), ^{167}Yb (p5n), ^{166}Tm (α3n), ^{165}Tm (α4n), ^{164}Tm (α5n), ^{162}Ho (2α3n), and ^{161}Ho (2α4n) were populated through CF and/or ICF channels in the system ^{19}F + ^{154}Sm at $E_{lab} \approx 78$–110 MeV. Statistical model (SM) calculations were performed using the code PACE-4 [21,22] to study the relative contributions of different ERs and estimate the contribution from any missing CF channel. The validity of the PACE-4 predictions for ER cross sections involving tightly bound projectiles is well tested [8–11]. Two important parameters in the SM calculations are (i) transmission coefficient of the outgoing particles and (ii) level density of the residual nuclei. The transmission coefficients for neutron and proton are calculated by using the optical model potentials of Becchetti and Greenlees [30], and the optical model of Satchler [31] is used for the emission of α particles. The level density parameter is $a = A/K$ MeV^{-1}, where A is the mass number of the residual nucleus and K is a free parameter. The nuclear data, such as half lives ($T_{1/2}$), γ ray energies (E_γ), and branching ratios (B_R) for the detected decay channels are given in Table I. The cross sections of different ER channels were obtained from the observed intensities of the γ lines as listed in Table I with branching ratios corresponding to both ground (g) and metastable (m) states of ERs.

The measured independent cross sections (σ_{expt}) of the ERs $^{169-167}$Lu and ^{167}Yb populated via xn ($x = 4, 5, 6$) and pxn ($x = 5$) emission channels were plotted along with PACE-4 predictions as a function of projectile energy and are displayed in Fig. 2. It can be observed from this figure that the measured cross sections of the ERs $^{169-167}$Lu, and ^{167}Yb are satisfactorily reproduced by the theoretical predictions of PACE-4 code at level density parameter constant $K = 10$. This indicates that these reaction channels are populated through only CF. The accelerated ^{19}F projectile entirely fuses with the ^{154}Sm target, leading to the formation of an excited compound nucleus (CN) ^{173}Lu*. This excited CN ^{173}Lu* further decays through the
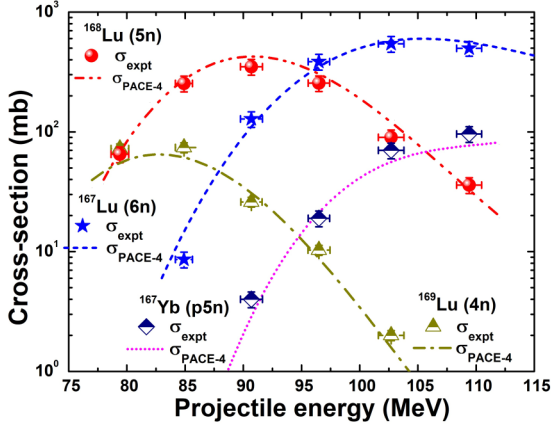
FIG. 2. Measured excitation functions of evaporation residues $^{169-167}$Lu, and ^{167}Yb populated via xn ($x = 4, 5, 6$) and pxn ($x = 5$) emission channels in the system ^{19}F $+$ ^{154}Sm at $E_{lab} \approx 78$–110 MeV. Different symbols represent the measured cross sections and dashed/dash-dotted curves represent the cross sections of PACE-4 code. the data points shown in figures include the errors and uncertainties.

emission of nucleons and γ rays forming the ERs $^{169-167}$Lu and ^{167}Yb via the emission of $4n$, $5n$, $6n$, and $p5n$ channels, respectively. As a representative case, formation of the ER ^{167}Yb through the $p5n$ channel may be given as

$$^{19}\text{F} + {}^{154}\text{Sm} \implies {}^{173}\text{Lu}^* \implies {}^{167}\text{Yb} + p5n.$$

The measured reaction cross sections of the observed ERs populated through xn, pxn, and α emitting channels in the ^{19}F $+$ ^{154}Sm reaction at $E_{lab} \approx 78$–110 MeV are listed in Tables II and III. Some of the residues were found to have contributions from their higher charge precursor isobars through electron capture or β decay, which were separated using the standard formulation [32]. The ERs $^{166-164}$Tm and ^{162,161}Ho associated with αxn ($x = 3, 4, 5$) and $2\alpha xn$ ($x = 3, 4$) emission channels may be populated through both CF and ICF dynamics. Since for xn/pxn channels the PACE-4 cross sections are well justified at the value of free parameter $K = 10$, the measured EFs of α emission channels were also compared with PACE-4 cross sections at K=10.

The measured independent cross sections for the ERs $^{166-164}$Tm and ^{162,161}Ho were plotted along with PACE-4 predictions and are shown in Fig. 3.

TABLE III. Measured cross sections of the observed ERs ^{164}Tm ($\alpha 5n$), ^{162}Ho ($2\alpha 3n$), and ^{161}Ho ($2\alpha 4n$) produced in the ^{19}F $+$ ^{154}Sm system at $E_{lab} \approx 78$–110 MeV.

E_{lab} (MeV)	^{164}Tm (mb)	^{162}Ho (mb)	^{161}Ho (mb)
79.4 $\pm$ 0.8			
84.9 $\pm$ 0.7			
90.7 $\pm$ 0.9	14 $\pm$ 1.4	2.68 $\pm$ 0.3	
96.5 $\pm$ 0.9	61.2 $\pm$ 6.1	6.5 $\pm$ 0.7	1.6 $\pm$ 0.2
102.7 $\pm$ 1.1	129 $\pm$ 12.9	15.9 $\pm$ 1.7	8.2 $\pm$ 1.0
109.4 $\pm$ 1.1	183.4 $\pm$ 18.3	18.6 $\pm$ 2.0	23.4 $\pm$ 2.8

As can be clearly seen from Fig. 3, the measured cross sections of these ERs are found to be much enhanced over their theoretical cross sections. These results suggest that the ERs associated with α emission channels are not only populated through CF, but they have also significant contributions from the ICF of the ^{19}F projectile with the ^{154}Sm target. The low α breakup threshold ($E_{\text{B.U.}}$) value of the ^{19}F projectile makes ICF or breakup fusion feasible, in which the incident projectile breaks up into fragments before fusion with the target nuclei. The ^{19}F projectile breaks up into $\alpha + {}^{15}$N under the influence of the target nuclear field, and the resulting breakup fragment ^{15}N further fuses with the ^{154}Sm target leading to the formation of the incompletely fused composite (IFC) system ^{169}Tm*. The α particle moves in the forward direction as spectator. As a representative case, the ER ^{166}Tm may be populated via the following different reaction routes:

(1) CF of ^{19}F with ^{154}Sm,

$$^{19}\text{F} + {}^{154}\text{Sm} \implies {}^{173}\text{Lu}^* \implies {}^{166}\text{Tm} + \alpha 3n.$$

(2) Only a part of the projectile ^{19}F (i.e., ^{15}N) fuses with the ^{154}Sm target to form the excited IFC system ^{169}Tm*. This composite system ^{169}Tm* may then decay to ^{166}Tm via emission of three neutrons, i.e.,

$$^{19}\text{F} ({}^{15}\text{N} + \alpha) \implies {}^{15}\text{N} + {}^{154}\text{Sm} \implies {}^{169}\text{Tm}^*$$
$$\implies {}^{166}\text{Tm} + 3n.$$
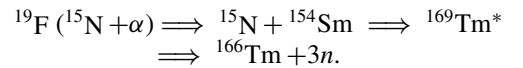
The ICF contribution in all α emission channels was deduced adopting the standard procedure [9–11]. The ICF cross sections for the ERs were deduced by subtracting the PACE-4 cross sections from the measured cross sections at each studied energy. Then, the ICF probability function, S_{ICF}, which is a measure of the strength of ICF, was deduced using the expression $S_{\text{ICF}} = \frac{\sigma_{\text{ICF}}}{\sigma_{\text{CF}} + \sigma_{\text{ICF}}} \times 100$.

TABLE II. Measured cross sections of the observed ERs ^{169}Lu ($4n$), ^{168}Lu ($5n$), ^{167}Lu ($6n$), ^{167}Yb ($p5n$), ^{166}Tm ($\alpha 3n$), and ^{165}Tm ($\alpha 4n$) produced in the ^{19}F $+$ ^{154}Sm system at $E_{lab} \approx 78$–110 MeV.

E_{lab} (MeV)	^{169}Lu (mb)	^{168}Lu (mb)	^{167}Lu (mb)	^{167}Yb (mb)	^{166}Tm (mb)	^{165}Tm (mb)
79.4 $\pm$ 0.8	72.3 $\pm$ 8.0	65.1 $\pm$ 7.2			6.8 $\pm$ 0.7	2.1 $\pm$ 0.2
84.9 $\pm$ 0.7	74.1 $\pm$ 8.2	254.3 $\pm$ 27.9	8.6 $\pm$ 0.9		14.3 $\pm$ 1.6	19.6 $\pm$ 1.9
90.7 $\pm$ 0.9	26.4 $\pm$ 2.9	350.7 $\pm$ 38.5	128.4 $\pm$ 12.8	4.2 $\pm$ 0.4	22 $\pm$ 2.4	53.4 $\pm$ 5.1
96.5 $\pm$ 0.9	10.3 $\pm$ 1.1	255.4 $\pm$ 28.1	386.5 $\pm$ 38.7	19.3 $\pm$ 1.9	18 $\pm$ 2.0	87.6 $\pm$ 8.3
102.7 $\pm$ 1.1	2.0 $\pm$ 0.2	90.1 $\pm$ 9.9	544.3 $\pm$ 54.4	70.8 $\pm$ 7.1	12 $\pm$ 1.3	111.7 $\pm$ 10.6
109.4 $\pm$ 1.1		36.2 $\pm$ 4.0	518.2 $\pm$ 51.8	96.5 $\pm$ 9.7	10.2 $\pm$ 1.1	97.8 $\pm$ 9.3

FIG. 3. Measured excitation functions of evaporation residues $^{166-164}$Tm and ^{162,161}Ho associated with αxn ($x = 3, 4, 5$) and $2\alpha\, xn$ ($x = 3, 4$) emission channels in the system ^{19}F + ^{154}Sm at $E_{\text{lab}} \approx 78$–110 MeV. Different symbols represent the measured cross sections and solid curves represent the cross sections of PACE-4 code. The data points shown in figures include the errors and uncertainties.

A. Critical angular momentum of CF from measured excitation functions

Formation of the excited compound system through either CF or ICF and its subsequent decay is governed by the quanta of angular momentum associated with the incident projectile. The ICF reactions occur mainly due to peripheral collisions [33], while in other works [34,35] ICF processes were found to be dominant reaction modes even at lower ℓ values. Prior studies [9–11] show that the ICF cross sections increase rapidly with projectile energy, while the CF cross sections continue to decrease at higher energy. This systematic behavior of the CF and total fusion (TF) cross sections has been considered by many investigators [36,37] as to a consequence of the critical angular momentum (ℓ_{crt}) associated with the compound system. As discussed earlier, the sum-rule model was proposed [38] to understand the role of entrance channel angular momentum involved in the CF and/or ICF processes. This model predicts that the ICF reactions predominantly occur in the ℓ space above the ℓ_{crt}. At ℓ values greater than ℓ_{crt}, the attractive pocket in the effective potential vanishes and hence the capture probability of the projectile by the target gets hindered. Consequently, the extra angular momentum is released in the form of breakup of projectile through the ICF process. At lower bombarding energies, the maximum angular momentum (ℓ_{max}) associated with the interacting system is close to the ℓ_{crt} value, thereby preventing any possibility of ICF reactions above ℓ_{crt}. The ℓ_{crt} can be well approximated by the equilibrium condition of the three forces, namely Coulomb, nuclear, and centrifugal

forces [37], as

$$2\pi(\gamma_P + \gamma_T)\frac{R_P R_T}{R_P + R_T} = \frac{Z_P Z_T e^2}{(R_P + R_T)^2} + \frac{\ell_{\text{crt}}(\ell_{\text{crt}} + 1)\hbar^2}{\mu(R_P + R_T)^3},$$
(2)

where μ is the reduced mass and R_P, R_T are the half-density radii, corresponding to the maximum attraction between the projectile and target. The surface tension coefficients γ_j were taken in the form

$$\gamma_j = 0.99\left[1 - 1.78\left(\frac{N_j - Z_j}{A_j}\right)^2\right] \text{MeV fm}^{-2}.$$
(3)

The CF cross section for the energy at which ℓ_{crt} is below the maximum angular momentum ℓ_{max} of the system may be given as

$$\sigma_{\text{CF}} = \pi\lambdabar^2 \sum_{\ell=0}^{\ell=\ell_{\text{crt}}} [2\ell + 1]T_\ell,$$
(4)

where $\lambdabar$ is reduced wavelength ($\lambdabar^2 = \frac{\hbar^2}{2\mu E_{\text{c.m.}}}$) and T_ℓ is the transmission coefficient for incident ℓ values. According to the sharp cutoff approximation [37], the transmission coefficient T_ℓ may be taken as

$$T_\ell = \begin{cases} 1 & \text{for } \ell \leqslant \ell_{\text{max}}, \\ 0 & \text{for } \ell > \ell_{\text{max}}, \end{cases}$$
(5)

where ℓ_{max} corresponds to the peripheral collisions and is given as

$$\ell_{\text{max}} = R\sqrt{2\mu(E_{\text{c.m.}} - V_{\text{CB}})/\hbar^2}.$$
(6)

TABLE IV. Measured CF cross sections (σ_{CF}^{expt}) along with ℓ_{crt} (fusion) derived from σ_{CF}^{expt}, ℓ_{crt} (CCFULL) calculated using the code CCFULL [40], and ℓ_{max} for the ^{19}F + ^{154}Sm system at different E_{lab} ($E_{c.m.}$) and the corresponding excitation energy (E^*).

E_{lab} ($E_{c.m.}$) (MeV)	E^* (MeV)	σ_{CF}^{expt} (mb)	ℓ_{crt} (fusion) ($\hbar$)	ℓ_{crt} (CCFULL) ($\hbar$)	ℓ_{max} ($\hbar$)
79.4 (70.7)	53.62	141.45	11	8	22
84.9 (75.6)	58.51	350.82	22	20	32
90.7 (80.7)	63.68	537.22	30	28	41
96.5 (85.9)	68.84	720.78	36	34	48
102.7 (91.4)	74.36	770.94	40	39	54
109.4 (97.4)	80.32	835.89	44	44	60

Here R is the maximum distance between the colliding nuclei at which the collision leads to a reaction, μ is the reduced mass, $E_{c.m.}$ is the center-of-mass energy of projectile, and V_{CB} is the fusion barrier of the system at a distance R.

The CF cross sections are needed for extraction of ℓ_{crt} values at each beam energy using Eq. (4). In these EF measurements, the activation technique was used for the identification of populated ERs. However, some of the ERs may not be detected owing to very long or short half-lives or no intense γ rays due to the limitation of this method. The cross sections of such ERs were incorporated using the statistical model code PACE-4. The branching of the sum of the measured channels (i.e., $\sigma_{xn/pxn}$) with respect to complete fusion (σ_{CF}) at each energy was calculated using PACE-4. The theoretical ratio of combined cross sections of these channels to the complete fusion $R_\sigma^{Theo} (= \sigma_{xn/pxn}/\sigma_{CF})$ is calculated for the ^{19}F + ^{154}Sm system. The neutron and/or proton evaporation channels are found to be dominant for the entire energy range in these measurements. The combined cross sections of xn/pxn channels are found to be in the range of 92%–94% of CF in the system ^{19}F + ^{154}Sm. The remaining contributions are mostly from the charged particle evaporation channels, which are difficult to extract from the measured γ lines as they are contaminated by the contributions from the transfer/ICF channels. In this respect, the experimental CF cross sections were calculated as $\sigma_{CF}^{expt} = \sigma_{xn/pxn}^{expt}/R_\sigma^{Theo}$ [39]. Hence, σ_{CF}^{expt} is the corrected total measured CF cross section, including contributions from all the observed and missing CF channels. The consistency in theoretical results for different ER channels was checked by using σ_{CF}^{expt} as an input to PACE-4. The results of σ_{CF}^{expt} and the extracted ℓ_{crt} values from σ_{CF}^{expt} data at each projectile energy for the ^{19}F + ^{154}Sm system are listed in Table IV. The ℓ_{crt} values obtained from the code CCFULL [40] are also shown in this table. It can be seen from this table that the ℓ_{crt} values deduced from the measured CF cross sections data are satisfactorily matched with the theoretical values obtained from CCFULL. The ℓ_{crt} values obtained from both the measured CF data and CCFULL were also found to lie below the ℓ_{max} values at particular bombarding energy, using Eq. (6). These observations show that the ICF reactions originate predominantly via peripheral collisions, involving the partial waves localized in the space between the ℓ_{crt} and ℓ_{max}.
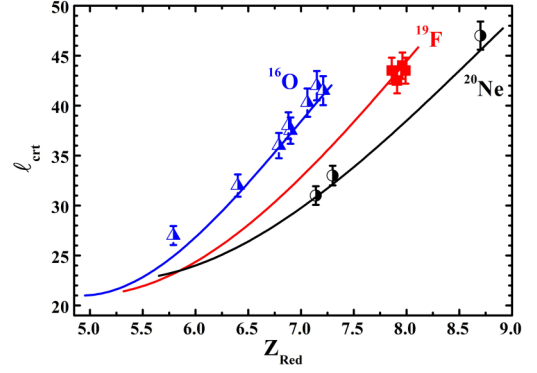
FIG. 4. Critical angular momentum (ℓ_{crt}) derived from the fusion cross sections for the ^{16}O (triangle), ^{19}F (square), and ^{20}Ne (circle) induced reactions as a function of reduced charge of the system at $E^* = 72$ MeV. Solid lines represents the prediction of the sum-rule model [37].

The influence of various entrance channel parameters in deciding the magnitude of the ℓ_{crt} for CF was further studied using the sum-rule model [38]. This model suggests that the ℓ_{crt} value of a system is influenced by the static properties, i.e., size and mass of the interacting partners. Hence, to study these aspects in more exclusive manner regarding the ℓ_{crt} and its dependence on entrance channel effects, the ℓ_{crt} values for the ^{20}Ne, ^{19}F and ^{16}O induced reactions with various targets were deduced using the sum-rule model and shown in Fig. 4 (solid curves) as a function of reduced charge [$Z_{Red} = Z_P Z_T/(Z_P + Z_T)$] of the system, where Z_P and Z_T are the atomic numbers of projectile and target, respectively. Further, the ℓ_{crt} values were also extracted from the measured CF cross sections using the standard formalism [37] at the excitation energy of 72 MeV for different systems [18–20,41–50] as given in Table V.

TABLE V. List of studied systems along with the breakup threshold energy ($E_{B.U.}$) of the projectile.

Projectile	$E_{B.U.}$ (MeV)	Target
^{20}Ne	4.73	^{55}Mn [41]
		^{59}Co [42]
		^{165}Ho [43]
^{19}F	4.01	^{154}Sm (present work)
		^{159}Tb [18]
		^{169}Tm [19]
		^{175}Lu [20]
^{16}O	7.16	^{45}Sc [44]
		^{74}Ge [44]
		^{103}Rh [45]
		^{115}In [46]
		^{124}Sn [47]
		^{148}Nd [48]
		^{165}Ho [49]
		^{181}Ta [50]
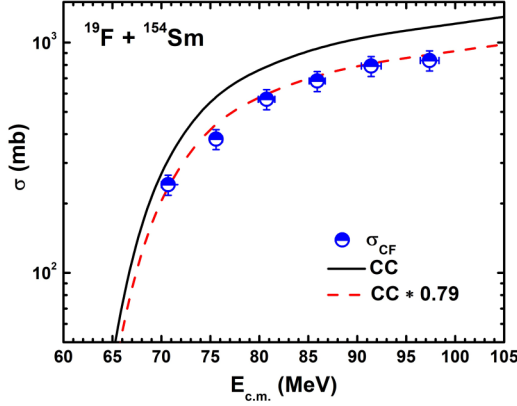
FIG. 5. Measured CF cross sections (circle) along with the CC-FULL calculations (solid line). The dashed line shows the CCFULL calculations scaled down by a factor of 0.79.

FIG. 6. Measured CF function $F(x)$ for the ^{19}F $+$ ^{154}Sm system (solid circle) along with the UFF (solid line). The dashed line shows the UFF scaled down by a factor of 0.79.

The ℓ_{crt} values deduced from the measured CF cross sections are shown by solid or half-filled symbols in Fig. 4. The projectiles ^{20}Ne, ^{19}F, and ^{16}O differ significantly from each other in terms of their $E_{\text{B.U.}}$ values as well as their structures. The ^{20}Ne and ^{16}O are $N = Z$ α cluster projectiles having fully 5α and 4α cluster structure with $E_{\text{B.U.}}$ values of 4.73 and 7.16 MeV, respectively. On the other hand, the ^{19}F projectile is $N \neq Z$ α clustered with $E_{\text{B.U.}}$ value of 4.01 MeV. As can be seen from Fig. 4, the ℓ_{crt} values increase gradually with the reduced charge for a given incident projectile. Moreover, the value of ℓ_{crt} was also found to depend on the $E_{\text{B.U.}}$ value of the incident projectile. For a given target (in the case of ^{20}Ne and ^{16}O projectiles), the higher the $E_{\text{B.U.}}$ value of the incident projectile, the lower is the corresponding ℓ_{crt} value of the system. Furthermore, in the case of the ^{19}F projectile, ℓ_{crt} values are larger than expected, despite the lower $E_{\text{B.U.}}$ value of the projectile. These observations indicate that the structure of the projectile plays a major role in governing the ICF process.

B. Influence of entrance channel effects on ICF strength function

To investigate the influence of various system parameters on ICF dynamics, coupled channels (CC) calculations were done using standard code CCFULL [40] for the ^{19}F $+$ ^{154}Sm system. The CC calculations performed by the code CCFULL do not consider the coupling to unbound or continuum states. Hence, in these calculations, the projectile breakup effect is not considered. To reproduce the fusion barrier, $V_B = 67.62$ MeV (Bass fusion barrier) obtained from the PACE-4 code, the values of the radius parameter r_0, nuclear potential depth V_0, and diffuseness parameter a were obtained using the Wood-Saxon parametrization of the Akyuz-Winther (AW) potential [51] in the CCFULL calculations. The values of V_0, r_0, and a, for the CC calculations were taken as 65.0 MeV, 1.18 fm, and 0.66 fm, respectively. These values were very close to the calculated values. The CCFULL calculations for the ^{19}F $+$ ^{154}Sm system (shown by the solid black line) are shown in Fig. 5 along with the measured CF cross sections (cir-

cles). As can be clearly seen in Fig. 5 that the measured CF cross sections are relatively lower than those obtained from the CCFULL calculations. The suppression in measured CF cross section from their CCFULL predictions is more significant at higher energies. However, the measured CF cross sections were reproduced by the CCFULL calculations multiplied by a factor of 0.79, as shown (by the red dashed line) in Fig. 5. Hence, it may be inferred from this comparison that the measured CF cross sections for the ^{19}F $+$ ^{154}Sm system got suppressed by approximately 21% as compared to the theoretical CCFULL calculations.
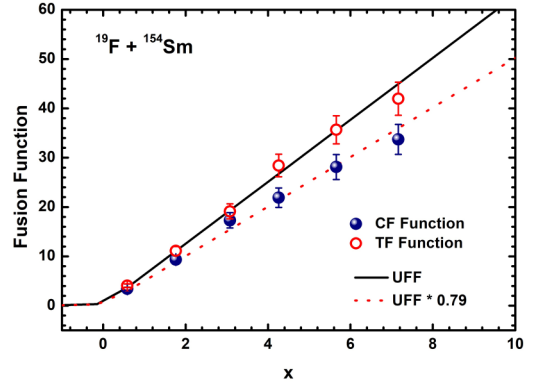
Further, an attempt was made to study the breakup effects of strongly bound projectile ^{19}F ($N \neq Z$ structure) on the fusion cross sections at energies above the Coulomb barrier. In this respect, a reduction procedure was adopted [23] that completely eliminates the geometrical and static effects of the potential acting between the interacting partners. Thus, any deviation of the measured CF function from the universal fusion function (UFF) may be due to the breakup of the incident projectile. The fusion cross section and the incident energy are reduced to a dimensionless equation called the fusion function $F(x)$ and dimensionless variable x in this reduction method:

$$F(x) = \frac{2E_{\text{c.m.}}}{\hbar \omega R_b^2} \sigma_{\text{CF}}, \quad x = \frac{E_{\text{c.m.}} - V_{\text{CB}}}{\hbar \omega}. \quad (7)$$

In these calculations, the potential parameters R_b, V_b, and $\hbar \omega$ used in the deduction of $F(x)$ and x were taken from the CCFULL calculations. The measured CF and total fusion (TF = CF + ICF) cross sections were reduced to the respective fusion functions derived from the Wong formula [52]. After simplification of the Wong formula, $F(x)$ reduces to

$$F_0(x) = \ln[1 + \exp(2\pi x)], \quad (8)$$

which is known as the universal fusion function (UFF). The measured CF function $F(x)$ with x (solid circles) for the ^{19}F $+$ ^{154}Sm system is shown in Fig. 6.

This figure clearly shows that the CF functions are suppressed compared to the UFF (solid black line). It was observed that the UFF scaled down by a factor of 0.79 (dashed line) shows good agreement with the CF functions. Thus, it can be concluded from the UFF calculations that the measured
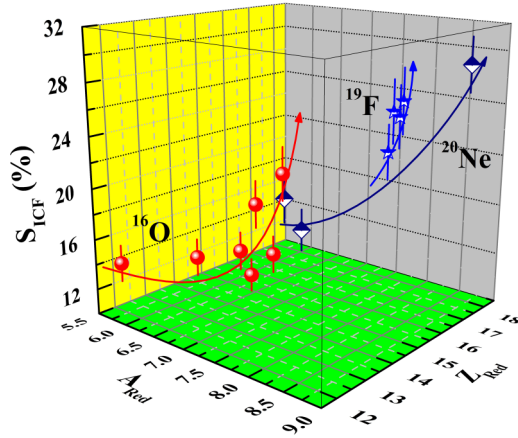
FIG. 7. Incomplete fusion strength function (S_{ICF}) as a function of reduced mass (A_{Red}) and reduced charge (Z_{Red}) for the ^{16}O, ^{19}F, and ^{20}Ne induced reactions.

FIG. 8. Incomplete fusion strength function (S_{ICF}) for the ^{16}O (triangle), ^{19}F (square), and ^{20}Ne (sphere) induced reactions as a function of reduced charge (Z_{Red}) of the system. Solid lines represent the calculations from the empirical formula [57] for the respective projectiles.

CF functions for the ^{19}F + ^{154}Sm system were suppressed by 21% with respect to UFF due to breakup of the incident projectile in the vicinity of the target nucleus. Further, the total fusion (TF) functions, which include the contribution of ICF cross sections also, were found to be satisfactorily matched with the UFF.

In this section, to study the influence of various parameters of entrance channel on ICF dynamics, the probability of ICF was deduced through ICF strength function for the present system, ^{19}F + ^{154}Sm. The S_{ICF} for the present system was compared with literature data [18–20,41–50] to perform a systematic investigation. The S_{ICF} deduced from the measured cross-sections was found to be in good agreement with the suppression in fusion cross section with respect to CCFULL or one-dimension barrier penetration model (1D-BPM) calculations. The effect of mass asymmetry on ICF was suggested by Morgenstern *et al.* [53], and since then many efforts [41–50] have been made to understand the role of various entrance channel parameters on ICF dynamics. It was shown in these studies that the mass-asymmetry and charge product play an important role in the reaction dynamics. In order to test the consistency of these aspects, the ICF probability was estimated by comparing the measured fusion cross section data with the CCFULL or 1D-BPM predictions for different systems. The ICF probability for several projectiles i.e., ^{16}O, ^{19}F, and ^{20}Ne induced reactions [18–20,41–50] including the present work was plotted as a function of reduced mass ($A_{Red} = A_P A_T / A_P + A_T$) and reduced charge [$Z_{Red} = Z_P Z_T / (Z_P + Z_T)$], as shown in Fig. 7. Here, A_P and A_T are the atomic masses of projectile and target, respectively. As can be seen from this figure, the variation of ICF fraction as a function of both reduced mass and charge shows an increasing pattern. The ICF probability for ^{19}F projectile is greater compared to ^{16}O, which may be due to its lower $E_{B.U.}$ value. These results show that the ICF probability (S_{ICF}) depends strongly on mass asymmetry as well as on Coulomb repulsion between the interacting partners, and increases with these parameters.
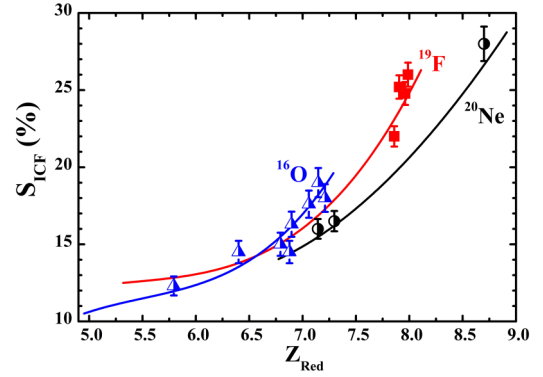
In recent years interest has grown for studies on fusion reactions induced by loosely and tightly bound projectiles [8–20,54–56]. The results of these studies were insufficient in establishing a systematic of fusion suppression and its dependency on the degree of various entrance channel effects. It is expected that increase in Z_T makes the Coulomb repulsion stronger between colliding nuclei. It means that the ICF probability also increases. The influence of Coulomb repulsion on fusion suppression was studied in detail [57]. From their analysis, they proposed an empirical formula for the prediction of S_{ICF} for different systems. The same formula was used to predict the S_{ICF} for various systems and compared with the measured data in this analysis. The S_{ICF} of 21% observed in the present ^{19}F + ^{154}Sm system was scaled to predict the S_{ICF} of ^{19}F induced reactions with any target as

$$S_{ICF} = S_{ICF}(^{154}Sm) \frac{V_N'}{V_N'(^{154}Sm)}$$

$$\times \exp\{-0.924[r_s - r_s(^{154}Sm)]\}. \quad (9)$$

All the quantities in Eq. (9) were calculated at the fusion barrier radius R_B calculated using the Sao Paulo potential [58]. The nuclear potentials for the ^{19}F induced reactions with different targets were calculated using the standard empirical formula [59]

$$V_N' = -50 \frac{R_P R_T}{R_P + R_T} \exp\left(\frac{-r_s}{0.63}\right), \quad (10)$$

where R_P is the radius of the projectile, R_T is the radius of the target, and r_s is the surface-to-surface separation. The value of r_s is approximated as $r_s = R_B - R(^{20}Ne) - R_T$. Similarly, the S_{ICF} of 18% observed in the case of ^{20}Ne [43] with ^{165}Ho target and 15% observed for ^{16}O [47] with ^{124}Sn target, were also scaled to predict the ICF probability for the ^{20}Ne and ^{16}O induced reactions with other targets listed in Table V. Figure 8 shows the variation of S_{ICF} as a function of Z_{Red} for the ^{20}Ne, ^{19}F, and ^{16}O induced reactions. Solid lines in Fig. 8 represent the empirical predictions [57] for the studied systems. It can be clearly observed from this figure that the S_{ICF} values increase gradually with the reduced charge for a given incident

projectile. However, the different rising rates of S_{ICF} values for different projectiles shows that the ICF strength function also depends on the $E_{B.U.}$ value of the incident projectile. For a given target (in case of ^{20}Ne and ^{16}O projectile), higher the $E_{B.U.}$ value of the incident projectile, lower is the corresponding S_{ICF} value of the system. Furthermore, in case of ^{19}F projectile, the S_{ICF} values are larger than expected, despite the lower $E_{B.U.}$ value of the projectile. These observations indicate that the structure and $E_{B.U.}$ value of projectile plays a critical role in determining the ICF contributions for different systems. It was also observed that, in general, the $N \neq Z$ α clustered projectile (like ^{19}F) will have lesser breakup probability than $N = Z$ α clustered projectile (^{20}Ne), while having similar values of α breakup thresholds $E_{B.U.}$.

IV. SUMMARY AND CONCLUSIONS

A study of the α cluster states in $N \neq Z$ nuclei ^{19}F has been studied through the offline γ ray measurements. The cross sections of evaporation residues for the ^{19}F + ^{154}Sm system have been measured above the Coulomb barrier. The measured partial cross sections for the evaporation residues populated via xn/pxn emission channels were found to be in good agreement with those derived employing statistical model calculations using the code PACE-4. Similar analysis of the fusion cross sections for the α emission channels shows significant enhancement over their PACE-4 predictions. The origin of the different behavior of the neutron and α channels may be attributed qualitatively to the incomplete fusion of ^{19}F. The measured complete fusion cross sections were found to be suppressed by $\approx$21% with respect to CCFULL calculations. Complete fusion functions extracted from measured complete fusion cross sections were compared with the universal fusion function. A similar value of suppression of complete fusion function was also observed. This suppression disappears with the inclusion of ICF functions.

The measured values of the incomplete fusion strength function (S_{ICF}) were found to be satisfactorily agreed with the empirical predictions deduced using prescriptions [57].

The S_{ICF} values were found to increase monotonically with the increase in reduced mass and reduced charge, indicating a significant role played by the mass asymmetry and Coulomb repulsion in the ICF dynamics. Moreover, the role of the α breakup threshold energy of the incident projectile was also reflected in this systematic study of S_{ICF}. The present study also points out that the $N \neq Z$ α clustered projectiles also have significant contributions of ICF on fusion cross sections at above barrier energies. However, the ICF probability for an $N \neq Z$ α clustered projectile (like ^{19}F) is found to be less than that of an $N = Z$ α clustered projectile (like ^{16}O and ^{20}Ne) with similar α breakup thresholds.

Incomplete fusion contribution and the suppression in complete fusion cross section for the $N \neq Z$ α clustered projectile have the same underlying cause. Weak binding leads to strong clustering and greater displacement of those clusters from the center of mass of the projectile. This makes the α amenable to transfer, and requires the center of mass of the ^{19}F projectile to get closer to the target to ensure that the entire projectile fuses. The former leads to incomplete fusion, and the latter to suppression of complete fusion. This interpretation should be valid for any projectile that shows strong clustering. These observations strongly suggest the presence of clustering in ^{19}F nuclei as α and ^{15}N. The studies of the clustering properties of ^{19}F can be useful as a probe of stellar nucleosynthesis. To establish the systematics of this effect, above-barrier no-capture breakup and singles α yields of reactions of $N \neq Z$ projectiles on a range of targets will be beneficial.

[1] M. L. Avila, G. V. Rogachev, V. Z. Goldberg, E. D. Johnson, K. W. Kemper, Yu. M. Tchuvil'sky, and A. S. Volya, Phys. Rev. C **90**, 024327 (2014).

[2] E. D. Johnson *et al.*, J. Phys.: Conf. Ser. **205**, 012011 (2010).

[3] K. P. Artemov, O. P. Belyanin, A. L. Vetoshkin, R. Wolskj, M. S. Golovkov, V. Z. Goldberg, M. Madeja, V. V. Pankratov, I. N. Serikov, V. A. Timofeev, V. N. Shadrin, and J. Szmider, Yad. Fiz. **52**, 634 (1990) [Sov. J. Nucl. Phys. **52**, 408 (1990)].

[4] A. K. Nurmukhanbetova, V. Z. Goldberg, D. K. Nauruzbayev, M. S. Golovkov, and A. Volya, Phys. Rev. C **100**, 062802(R) (2019).

[5] M. La Cognata *et al.*, Astrophys. J. **739**, L54 (2011).

[6] M. La Cognata *et al.*, J. Phys.: Conf. Ser. **1668**, 012023 (2020).

[7] D. Torresi, C. Wheldon, T. Kokalova, S. Bailey, A. Boiano, C. Boiano, M. Fisichella, M. Mazzocco, C. Parascandolo, D. Pierroutsakou, E. Strano, M. Zadro, M. Cavallaro, S. Cherubini, N. Curtis, A. DiPietro, J. P. FernandezGarcia, P. Figuera, T. Glodariu, J. Grebosz, M. LaCognata, M. LaCommara, M.

Lattuada, D. Mengoni, R.G. Pizzone, C. Signorini, C. Stefanini, L. Stroe, and C. Spitaleri, Phys. Rev. C **96**, 044317 (2017).

[8] S. Ali, K. Kumar, M. Gull, T. Ahmad, I. A. Rizvi, A. Agarwal, A. K. Chaubey, and S. S. Ghugre, Phys. Rev. C **100**, 064607 (2019).

[9] A. Mahato *et al.*, Eur. Phys. J. A **56**, 131 (2020).

[10] D. Singh, R. Ali, M. Afzal Ansari, B. S. Tomar, M. H. Rashid, R. Guin, and S. K. Das, Phys. Rev. C **83**, 054604 (2011).

[11] S. A. Tali, H. Kumar, M. A. Ansari, A. Ali, D. Singh, R. Ali, P. K. Giri, S. B. Linda, R. Kumar, S. Parashari, S. Muralithar, and R. P. Singh, Phys. Rev. C **100**, 024622 (2019).

[12] H. Kumar, S. A. Tali, M. Afzal Ansari, R. Ali, D. Singh, M. P. N. Naseef, R. Kumar, K. S. Golda, R. P. Singh, and S. Muralithar, Indian J. Pure Appl. Phys. **57**, 540 (2019).

[13] P. K. Giri, A. Mahato, D. Singh, S. B. Linda, H. Kumar, S. A. Tali, M. A. Ansari, R. Kumar, S. Muralithar, and R. P. Singh, Phys. Rev. C **100**, 054604 (2019).

[14] D. Singh *et al.*, Phys. Lett. B **774**, 7 (2017).

[15] D. Singh, S. B. Linda, P. K. Giri, A. Mahato, R. Tripathi, H. Kumar, M. A. Ansari, N. P. M. Sathik, R. Ali, R. Kumar, S. Muralithar, and R. P. Singh, Phys. Rev. C **97**, 064604 (2018).

[16] D. Singh *et al.*, Eur. Phys. J. A **55**, 1 (2019).

[17] R. Ali *et al.*, Nucl. Phys. A **968**, 403 (2017).

[18] Mohd. Shuaib, V. R. Sharma, A. Yadav, P. P. Singh, M. K. Sharma, D. P. Singh, R. Kumar, R. P. Singh, S. Muralithar, B. P. Singh, and R. Prasad, Phys. Rev. C **94**, 014613 (2016).

[19] Mohd. Shuaib *et al.*, J. Phys. G: Nucl. Part. Phys. **44**, 105108 (2017).

[20] Mohd. Shuaib, V. R. Sharma, A. Yadav, M. K. Sharma, P. P. Singh, D. P. Singh, R. Kumar, R. P. Singh, S. Muralithar, B. P. Singh, and R. Prasad, Phys. Rev. C **98**, 014605 (2018).

[21] A. Gavron, Phys. Rev. C **21**, 230 (1980).

[22] O. B. Tarasov and D. Bazin, Nucl. Instrum. Methods Phys. Res., Sect. B **266**, 4657 (2008).

[23] L. F. Canto *et al.*, Nucl. Phys. A **821**, 51 (2009).

[24] G. K. Mehta and A. R Patro, Nucl. Instrum. Methods Phys. Res., Sect. A **268**, 334 (1988).

[25] D. Kanjilal *et al.*, Nucl. Instrum. Methods Phys. Res., Sect. A **328**, 97 (1993).

[26] Pankaj K. Giri, A. Mahato, D. Singh, S. B. Linda, Abhilash S. R., N. K Deb, G. R. Umapathy, S. Ojha, D. Kabiraj, and S. Chopra, Indian J. Pure & Appl. Phys. **57**, 675 (2019).

[27] S. Y. F. Chu, L. P. Ekstrom, and R. B. Firestone, The Lund/LBNL Nuclear Data Search, LBNL, Berkeley, CA, Version 2.0, 1999, http://nucleardata.nuclear.lu.se/toi/index.asp

[28] National Nuclear Data Center, Brookhaven National Laboratory, https://www.nndc.bnl.gov/chart/chartNuc.jsp

[29] M. Afzal Ansari *et al.*, Ann. Nucl. Energy **11**, 607 (1984).

[30] F. D. Becchetti and G. W. Greenlees, Phys. Rev. **182**, 1190 (1969).

[31] G. R. Satchler, Nucl. Phys. **70**, 177 (1965).

[32] M. Cavinato, E. Fabrici, E. Gadioli, E. Gadioli Erba, P. Vergani, M. Crippa, G. Colombo, I. Redaelli, and M. Ripamonti, Phys. Rev. C **52**, 2577 (1995).

[33] W. Trautmann, O. Hansen, H. Tricoire, W. Hering, R. Ritzka, and W. Trombik, Phys. Rev. Lett. **53**, 1630 (1984).

[34] H. Tricoire, Z. Phys. A **312**, 221 (1983).

[35] R. L. Robinson, R. L. Auble, I. Y. Lee, M. J. Martin, G. R. Young, J. Gomez del Campo, J. B. Ball, F. E. Bertrand, R. L. Ferguson, C. B. Fulmer, J. R. Wu, J. C. Wells, and H. Yamada, Phys. Rev. C **24**, 2084 (1981).

[36] M. Blann and F. Plasil, Phys. Rev. Lett. **29**, 303 (1972).

[37] J. Wilczynski, Nucl. Phys. A **216**, 386 (1973).

[38] J. Wilczynski *et al.*, Nucl. Phys. A **373**, 109 (1982).

[39] C. S. Palshetkar, S. Santra, A. Chatterjee, K. Ramachandran, S. Thakur, S. K. Pandit, K. Mahata, A. Shrivastava, V. V. Parkar, and V. Nanal, Phys. Rev. C **82**, 044608 (2010).

[40] K. Hagino *et al.*, Comput. Phys. Commun. **123**, 143 (1999).

[41] R. Ali *et al.*, J. Phys. G: Nucl. Part. Phys. **37**, 115101 (2010).

[42] D. Singh *et al.*, Nucl. Phys. A **981**, 75 (2019).

[43] D. Singh *et al.*, Nucl. Phys. A **879**, 107 (2012).

[44] D. Singh *et al.*, J. Phys. Soc. Jpn. **82**, 114201 (2013).

[45] U. Gupta *et al.*, Nucl. Phys. A **811**, 77 (2008).

[46] K. Kumar, T. Ahmad, S. Ali, I. A. Rizvi, A. Agarwal, R. Kumar, and A. K. Chaubey, Phys. Rev. C **88**, 064613 (2013).

[47] D. Singh, S. B. Linda, P. K. Giri, A. Mahato, R. Tripathi, H. Kumar, S. A. Tali, S. Parashari, A. Ali, R. Dubey, M. A. Ansari, R. Kumar, S. Muralithar, and R. P. Singh, Phys. Rev. C **97**, 064610 (2018).

[48] P. K. Giri, D. Singh, A. Mahato, S. B. Linda, H. Kumar, S. A. Tali, S. Parasari, A. Ali, M. A. Ansari, R. Dubey, R. Kumar, S. Muralithar, and R. P. Singh, Phys. Rev. C **100**, 024621 (2019).

[49] K. Kumar, T. Ahmad, S. Ali, I. A. Rizvi, A. Agarwal, R. Kumar, K. S. Golda, and A. K. Chaubey, Phys. Rev. C **87**, 044608 (2013).

[50] D. P. Singh, Unnati, P. P. Singh, A. Yadav, M. K. Sharma, B. P. Singh, K. S. Golda, R. Kumar, A. K. Sinha, and R. Prasad, Phys. Rev. C **80**, 014601 (2009).

[51] O. Akyüz and A. Winther, in *Proceedings of the International School of Physics Enrico Fermi, Course LXXVII*, edited by R. A. Broglia, R. A. Ricci, and C. H. Dasso (North-Holland, Amsterdam, 1981), p. 492.

[52] C. Y. Wong, Phys. Rev. Lett. **31**, 766 (1973).

[53] H. Morgenstern, W. Bohne, W. Galster, K. Grabisch, and A. Kyanowski, Phys. Rev. Lett. **52**, 1104 (1984).

[54] N. Keeley *et al.*, Prog. Part. Nucl. Phys. **59**, 579 (2007).

[55] P. K. Rath, S. Santra, N. L. Singh, R. Tripathi, V. V. Parkar, B. K. Nayak, K. Mahata, R. Palit, S. Kumar, S. Mukherjee, S. Appannababu, and R. K. Choudhury, Phys. Rev. C **79**, 051601(R) (2009).

[56] V. V. Parkar, R. Palit, S. K. Sharma, B. S. Naidu, S. Santra, P. K. Joshi, P. K. Rath, K. Mahata, K. Ramachandran, T. Trivedi, and A. Raghav, Phys. Rev. C **82**, 054601 (2010).

[57] D. J. Hinde, M. Dasgupta, B. R. Fulton, C. R. Morton, R. J. Wooliscroft, A. C. Berriman, and K. Hagino, Phys. Rev. Lett. **89**, 272701 (2002).

[58] M. A. Cândido Ribeiro, L.C. Chamon, D. Pereira, M. S. Hussein, and D. Galetti, Phys. Rev. Lett. **78**, 3270 (1997).

[59] P. R. Christensen and A. Winther, Phys. Lett. B **65**, 19 (1976).